



1 **Representation of the Autoconversion from Cloud to Rain Using a**
2 **Weighted Ensemble Approach**

3

4 **Jinfang Yin^{1*}, Xudong Liang¹, Hong Wang², Haile Xue¹**

5

6 1 State Key Laboratory of Severe Weather (LaSW), Chinese Academy of

7 Meteorological Sciences (CAMS), Beijing 100081, China

8 2 Guangzhou Institute of Tropical and Marine Meteorology, China Meteorological

9 Administration (CMA), Guangzhou 510080, China

10

11

12

13

14 *Corresponding to:* Jinfang Yin (yinjf@cma.gov.cn)



15 **Abstract.** Cloud and precipitation processes remain among the largest sources of
16 uncertainties in weather and climate modeling, and considerable attention has been
17 paid to improve the representation of the cloud and precipitation processes in
18 numerical models in the last several decades. In this study, we develop a weighted
19 ensemble (named as EN) scheme by employing several widely used autoconversion
20 (ATC) schemes to represent the ATC from cloud water to rainwater. One unique
21 feature of the EN approach is that ATC rate is a weighted mean value based on the
22 calculations from several ATC schemes within a microphysics scheme with a
23 negligible increase of computation cost. The EN scheme is compared with the several
24 commonly used ATC schemes by performing a real case simulations. In terms of
25 accumulated rainfall and extreme hourly rainfall rate, the EN scheme provides better
26 simulations than that by using the single Berry-Reinhardt scheme which was
27 originally used in the Thompson scheme. It is worth emphasizing, in the present study,
28 we only pay our attention to the ATC process from cloud water into rainwater with the
29 purpose to improve the modeling of the extreme rainfall events over southern China.
30 Actually, any (source/sink) term in a cloud microphysics scheme can be dealt with the
31 same approach. The ensemble method proposed herein appears to have important
32 implications for developing cloud microphysics schemes in numerical models,
33 especially for the models with variable grid resolution, which would be expected to
34 improve of the representation of cloud microphysical processes in the weather and
35 climate models.



36 **1 Introduction**

37 Cloud and precipitation processes and associated feedbacks have been confirmed to
38 cause the largest uncertainties in weather and climate modeling by the Intergovernmental
39 Panel on Climate Change (IPCC) ([Houghton et al., 2001](#)). Owing to the complex
40 microphysical processes in clouds and their interactions with dynamical and thermodynamic
41 processes, considerable attention has been devoted to developing cloud microphysics schemes
42 in the numerical weather and climate models in the last several decades, which is summarized
43 in several review articles (e.g., [Grabowski et al., 2019](#); [Khain et al., 2015](#); [Morrison et al.,](#)
44 [2020](#)). Because of fundamental gaps in the knowledge of cloud microphysics, however, there
45 are still a large number of empirical values derived and assumptions in microphysics schemes
46 based on limited observations, even from numerical simulations ([Tapiador et al., 2019](#)). As a
47 result, simulations are quite sensitive to microphysical parameter settings ([Falk et al., 2019](#);
48 [Freeman et al., 2019](#); [Gilmore et al., 2004](#)), and thus obvious differences occur frequently
49 from different simulations due to the poor representation of the empirical values and
50 assumptions ([Lei et al., 2020](#); [White et al., 2017](#)).

51 Collision–coalescence between cloud droplets forming raindrops is named as the
52 autoconversion (ATC), which is a significant microphysical process in warm clouds. Therefore,
53 representation of the ATC from cloud water to rainwater is a key aspect of cloud microphysical
54 parameterization. Firstly, raindrop is initiated by ATC process in warm clouds, which plays a
55 significant role in the onset of a rainfall event. Besides, ATC process has important influence on
56 cloud microphysical properties by bridging aerosols, cloud droplets, and raindrops ([White et al.,](#)



57 [2017](#)). Additionally, local circulation may be modified to a certain extent due to falling down
58 of the initialized raindrops because of terminal velocity of raindrop ([Doswell, 2001](#)).
59 Moreover, changes in the rate of ACT had some effect on the lower-tropospheric radiative
60 flux divergence (Grabowski et al., 1999). Consequently, an appropriate representation of the
61 ATC process is helpful for our understanding of cloud micro- and macro-properties, as well as
62 precipitation processes.

63 Over the last several decades, much attention has been devoted to establishing ATC
64 schemes in atmospheric numerical models, and efforts are under way to create accurate and
65 computationally efficient ATC schemes. Kessler ([1969](#)) pioneered a simple scheme in which
66 the ATC rate was connected to cloud water content (CWC), and the scheme has been widely
67 used in bulk microphysics schemes (e.g., [Chen and Sun, 2002](#); [Dudhia, 1989](#); [Ghosh and Jonas,](#)
68 [1999](#); [Rutledge and Hobbs, 1984](#)). As an alternate way, Berry ([1968](#)) established a more
69 physical formulation in which not only CWC was considered but also cloud droplet number
70 concentration (N_c) and spectral shape parameter of cloud droplet size distribution. The Berry
71 scheme was featured by estimating the time t required for the sixth-moment diameter of the
72 spectral density to reach 80 μm by droplet coalescence, and Simpson and Wiggert ([1969](#))
73 increased the sixth-moment diameter to 100 μm . Ghosh and Jonas ([1999](#)) proposed a scheme
74 by combining the advantages of the Kessler and Berry schemes, which allow the use of the
75 simple linear Kessler-type expression and incorporating the effects of different cloud types. On
76 the other hand, several model-derived empirical schemes was established on the basis of
77 sophisticated microphysical simulations ([Berry and Reinhardt, 1974](#); [Franklin, 2008](#);
78 [Khairoutdinov and Kogan, 2000](#); [Lee and Baik, 2017](#)). Recently, Some studies (e.g., [Franklin,](#)



79 [2008](#); [Li et al., 2019](#); [Onishi et al., 2015](#); [Seifert et al., 2010](#)) the effect of turbulence on ATC
80 have been taken into account. Naeger et al. [\(2020\) proposed that](#) a neglect of turbulence
81 influence within a ATC scheme resulted in very weak condensational and collisional growth
82 processes, and thus underpredicted the contribution of warm rain processes to the surface
83 precipitation. More recently, multi-moment schemes were explored, which appeared to
84 improve precipitation simulation in a certain extent ([Kogan and Ovchinnikov, 2019](#)).

85 To date, numerous of ATC schemes have been established ([Beheng, 1994](#); [Berry, 1968](#);
86 [Berry and Reinhardt, 1974](#); [Caro et al., 2004](#); [Franklin, 2008](#); [Kessler, 1969](#); [Kogan and](#)
87 [Ovchinnikov, 2019](#); Lee and Baik, 2017; [Lin et al., 2002](#); [Liu and Daum, 2004](#); [Liu et al., 2006](#);
88 [Manton and Cotton, 1977a](#); [Seifert and Beheng, 2001](#); [Wood et al., 2002](#); [Yin et al., 2015](#)). As
89 were noted in previous studies ([Gilmore and Straka, 2008](#); [Hsieh et al., 2009](#); [Liu et al., 2006](#);
90 [Xiao et al., 2020](#); [Yin et al., 2015](#)), ATC rates predicted by different schemes can differ by
91 several orders of magnitude for a given CWC. Many previous studies have shown that ATC
92 rates are often overestimated/underestimated by those ATC schemes. For instance, Cotton
93 [\(1972\)](#) pointed out that the Kessler's formulation produced the largest error at smaller CWCs,
94 and Berry's formulation consistently resulted in a low rain rate low in the simulated clouds.
95 Iacobellis and Somerville [\(2006\)](#) proposed that the Manton-Cotton parameterization ([Manton](#)
96 [and Cotton, 1977b](#)) produced much larger values of liquid water path (LWP) than
97 measurements both by satellites and surface-based at the Atmospheric Radiation Measurement
98 (ARM) Program's Southern U.S. Great Plains site. Silverman and Glass [\(1973\)](#) addressed
99 that the Cotton [\(1972\)](#) scheme resulted in a peak cloud water content that was in lowest in value,
100 occurred earliest in time, and occurred at the lowest height in clouds, compared to those of the



101 Kessler ([1969](#)), Berry ([1968](#)), and Simpson-Wiggert ([1969](#)) schemes. However, Flatøy ([1992](#))
102 stated that Sundqvist's ([Sundqvist et al., 1989](#)) and Kessler's ([Kessler, 1969](#)) schemes gave
103 comparable results when used a suitable choice of parameters. To the best of our knowledge,
104 however, there is no one ATC parameterization scheme able to provide good results at all times
105 so far, and much effort is necessary for further development of the ATC parameterization
106 ([Michibata and Takemura, 2015](#)).

107 As noted by Morrison et al. ([2020](#)), one of the most serious issues of treating
108 microphysics in weather and climate models is the uncertainties in the microphysical process
109 rates owing to fundamental gaps in the knowledge of cloud physics. Posselt et al. ([2019](#))
110 proposed that changes in cloud microphysical parameters produced the same order of
111 magnitude change in model output as did changes to initial conditions, and thus it was
112 important to constraint uncertainties in cloud microphysical processes if possible. Wellmann
113 et al. ([2020](#)) also pointed out that model dynamical and microphysical properties were
114 sensitive to both the environmental and microphysical uncertainties, and the latter resulted in
115 larger uncertainties in the output of integrated hydrometeor mass contents and precipitation
116 variables.

117 There is still poor representation of ATC process in weather and climate models, and the
118 potential uncertainties are non-negligible in the ATC schemes ([Michibata and Takemura,](#)
119 [2015](#)), and continued advancement of parameterizations are require greater knowledge of the
120 underlying physical processes in order to reduce the uncertainties, including from laboratory
121 studies, cloud observations, and detailed process modeling ([Randall et al., 2019](#)). Most
122 importantly, representing cloud processes consistently across multi-scales models with an



123 empirical scheme appears to be one of the major challenges in the cloud parameterizations
124 ([Randall et al., 2019](#)). To fill this gap, the objective of this paper is to address how to reduce the
125 negative effects of inherent uncertainties in the ATC (from cloud water to rainwater)
126 parameterization within a cloud microphysics scheme to make the weather and climate models
127 behave realistically. To achieve this goal, we design a weighted ensemble (herein abbreviated
128 as EN) scheme to represent the ATC process by employing several widely used ATC schemes
129 within a cloud microphysics scheme.

130 This paper is organized as follows. An overview of the selected ATC schemes is presented
131 in Section 2. Section 3 describes the approach of ensemble scheme. The Weather Research and
132 Forecasting (WRF) model configuration and experiment settings are given in Section 4.
133 Simulated results of an extreme rainfall event are presented in Section 5. Finally, conclusion
134 and discussions are given in Section 6.

135 **2 Overview of the selected autoconversion schemes**

136 In the present study, four widely used ATC schemes are selected, including Kessler ([1969](#))
137 (KE) scheme, Berry and Reinhardt ([1974](#)) (BR) scheme, Khairoutdinov and Kogan ([2000](#))
138 (KK) scheme, and Liu et al. ([2006](#)) (LD) scheme. Depending on properties of the “bulk”
139 microphysics schemes, the KE scheme is a one-moment scheme, and the BR and KK are
140 double-moment schemes. The LD scheme provides a generalized expression with smooth
141 transition in the vicinity of the ATC threshold, which is featured by eliminating unnecessary
142 assumptions inherent in the existing Kessler-type parameterizations. It should be noted it is
143 still troublesome to justify in recommending one of the ATC schemes over the other, although



144 those schemes have been extensively tested and widely used in the previous studies ([Gilmore](#)
145 [and Straka, 2008](#); [Jing et al., 2019](#); [Michibata and Takemura, 2015](#); [White et al., 2017](#)).

146 **2.1 Kessler (KE) scheme**

147 Kessler ([1969](#)) pioneered a simple expression in which ATC rate is related to CWC. The
148 KE scheme has been widely used in cloud-related processes in weather and climate numerical
149 models due to its simplicity. The ATC rate from cloud water to rainwater is expressed as

$$150 \quad P_{ATC-KE} [\text{kg kg}^{-1} \text{ s}^{-1}] = r_a a (q_c - q_0) H(q_c - q_0) \begin{cases} q_c - q_0 \geq 0, H(q_c - q_0) = 1, \\ q_c - q_0 < 0, H(q_c - q_0) = 0. \end{cases} \quad (1)$$

151 where $a = 0.001 \text{ s}^{-1}$ is a time constant, H is the Heaviside function, q_c is CWC in unit of kg
152 m^{-3} , and r_a is air density. The threshold q_0 is the minimum CWC below which there is no
153 ATC from cloud water to rainwater (Fig. 1a). Owing to the simple and linear expression, the
154 KE scheme is computationally straightforward to implement in numerical models. However,
155 the major limitation of the KE scheme results in its inability to identify different conditions
156 such as maritime and continental clouds ([Ghosh and Jonas, 1999](#)). Besides, it is impossible to
157 obtain the thresholds directly used in the scheme from observations at present, while cloud
158 microphysical processes are sensitive to the thresholds (Plisselt et al., 2019). A modified
159 Kessler scheme was proposed by Yin et al. ([2015](#)) in which q_0 is diagnosed as a function of
160 altitude by using a CWC-height relationship which was derived from CloudSat observations.
161 In fact, different values of q_0 were chosen by various studies. For instance, a value of 0.5 g
162 m^{-3} is given in Kessler's ([1969](#)), Reisner ([1998](#)), and Schultz ([1995](#)). Thompson ([2004](#))
163 reduced to a small value of 0.35 g m^{-3} . Kong and Yau ([1997](#)) and Tao and Simpson ([1993](#))
164 gave a value of 2 g kg^{-1} , while a small value of 0.7 g kg^{-1} was assigned in Chen and Sun



165 (2002). In this work, the same value of 0.5 g m^{-3} as that assigned in Kessler's (1969) is
166 chosen.

167 2.2 Berry-Reinhardt (BR) scheme

168 Berry and Reinhardt (1974) proposed an physical formulation to represent ATC process in
169 clouds, which is given by

$$170 P_{ATC-BR} [\text{kg kg}^{-1} \text{ s}^{-1}] = \frac{2.7 \times 10^{-2} r_w q_c \left[\frac{1}{16} \times 10^{20} D_{mean}^4 (1+m)^{-0.5} - 0.4 \right]}{\frac{3.7}{r_a q_c} \left[0.5 \times 10^6 D_{mean} (1+m)^{-1/6} - 7.5 \right]^{-1}}. \quad (2)$$

171 Here, m represents shape parameter of a gamma distribution, r_w is liquid water density. D_{mean}
172 is the mean diameter (unit in m) of the total cloud droplets, which is computed from

$$173 D_{mean} = \left(\frac{6q_c}{pr_w N_c} \right)^{1/3}. \quad (3)$$

174 Here, p is the circumference ratio. Compared to KE, the BR scheme has treated the process
175 more rigorously (Ghosh and Jonas, 1999). It should be noted that ATC rates given by BR are
176 quite sensitive to N_c (Fig. 1b).

177 2.3 Khairoutdinov-Kogan (KK) scheme

178 Khairoutdinov and Kogan (2000) proposed a computationally efficient and relatively
179 simple scheme, which aims at large-eddy simulation (LES). One of the advantages is that there
180 is no need to define a threshold, and this scheme has been broadly used in numerical models
181 (e.g., Morrison et al., 2009). The ATC rate is given by

$$182 P_{ATC-KK} [\text{kg kg}^{-1} \text{ s}^{-1}] = 1350 q_c^{2.47} (N_c \times 10^{-6})^{-1.79}. \quad (4)$$

183 The KK scheme uses a simple power law expression based on bin microphysical calculations.

184 The simple expression is a key advantage of the KK scheme, which makes it possible to



185 analytically integrate the microphysical process rates over a probability density function
186 ([Griffin and Larson, 2013](#)). In view of Fig. 1c, the KK scheme has a strong dependency on N_c .
187 Increasing N_c from 100 to 500, ATC rates decreases dramatically, especially at the CWCs over
188 1.0 g m^{-3} . Unlike the KE scheme, ATC is allowable in the KK scheme even very low CWCs.

189 **2.4 Liu-Daum-McGraw-Wood (LD) scheme**

190 A generalized ATC parameterization was proposed by Liu et al. ([2006](#)). The approach
191 improved the representation of the threshold function by applying the expression for the critical
192 radius derived from the kinetic potential theory. The parameterization is given by

$$193 \quad P_{ATC-LD}[\text{kg kg}^{-1} \text{ s}^{-1}] = kb^6 q_c^3 N_c^{-1} \{1 - \exp[-(1.03 \times 10^{16} N_c^{-3/2} q_c^2)^m]\}. \quad (5)$$

194 Here, $\kappa (=1.1 \times 10^{10} \text{ kg}^{-2} \text{ m}^3 \text{ s}^{-1})$ is a constant. β is a parameter related to relative dispersion e of
195 cloud droplets, which is obtained from

$$196 \quad b = \left[\frac{(1 + 3e^2)(1 + 4e^2)(1 + 5e^2)}{(1 + e^2)(1 + 2e^2)} \right]^{\frac{1}{6}}. \quad (6)$$

197 Here, a value of 0.5 is assigned to e following Liu et al. (2006). The LD scheme is
198 characterized by the smooth transition in the vicinity of the ATC threshold.

199 **3 Description of the ensemble (EN) scheme**

200 As has been mentioned above, ATC rates predicted by different schemes can differ by
201 several orders of magnitude for a given CWC. Nowadays, it is still troublesome to judge which
202 scheme is preferred to others at all times ([Ghosh and Jonas, 1999](#); [Jing et al., 2019](#); [Liu et al.,](#)
203 [2006](#); [Michibata and Takemura, 2015](#)). To the best of our knowledge, each one has its own
204 advantages and disadvantages. Keeping this fact in our mind, we propose a weighted the EN
205 scheme by employing the above-listed four commonly used ATC schemes, and the weighted



206 ensemble ATC rate (P_{ATC-EN}) is given by

$$207 \quad P_{ATC-EN} [\text{kg kg}^{-1} \text{ s}^{-1}] = \frac{w_{KE} P_{ATC-KE} + w_{KK} P_{ATC-KK} + w_{LD} P_{ATC-LD} + w_{BR} P_{ATC-BR}}{w_{KE} + w_{KK} + w_{LD} + w_{BR}}. \quad (7)$$

208 Here, w_{xx} , referring to that for KE, KK, LD, and BR, respectively, is the weight of each ATC
209 scheme. It is worth noting that Eq. (7) is easily reduced into any single scheme form by setting all
210 w_{xx} values of 0 except for one of them. Therefore, it is a flexible way to use any one or more
211 schemes to calculate P_{ATC-EN} by adjusting w_{xx} . Of course, it is also convenient to reduce the
212 effect of any one of them by giving a small value of w_{xx} . At present, the same weights with the
213 value of 1.0 are assigned for all schemes for simplicity. Note that, the weights can be modulated
214 according to weather conditions. One of the features of the EN scheme is that the weighted
215 mean is calculated within a microphysics scheme, and the increasing of computation cost is
216 negligible.

217 Similar to an ensemble prediction system (Lewis, 2005), the EN scheme is expected to
218 reduce the potential uncertainties from the use of any ATC scheme alone under various CWC
219 conditions. For example, no cloud water converts into rain water in the KS scheme when the
220 cloud water is less than the threshold, while in the KK scheme it always occurs. However, the
221 KS scheme has much higher ATC rates owing to the linear relationship (Eq. 1), compared to
222 those of the KK scheme. Most importantly, the EN scheme is beneficial for the multi-scale
223 numerical weather and climate modeling systems, especially for variable resolution models
224 (e.g., the Model for Prediction Across Scales, MPAS (Skamarock et al., 2012), the
225 Global-to-Regional Integrated forecast SysTem, GRIST, (Zhang et al., 2019)), because it is
226 flexible to represent subgrid-scale cloud processes consistently across all model scales under
227 the various conditions. Depending on grid distance, one or more schemes can be used



228 independently in a variable resolution model. For example, we assign all w_{xx} to 0 except for
229 w_{KK} in fine grid distance region, and a mean value from the calculation of two or more
230 schemes is utilized in the grid distance transition zone.

231 To facilitate comparisons among the aforementioned ATC schemes, an idealized
232 experiment is performed with a wide range of CWCs in the calculations. A roughly value of N_c
233 is set to 300 cm^{-3} in the continental clouds (e.g., Hong and Lim, 2006; Thompson et al., 2008).
234 For convenience, air density is approximately fixed at $1.29 \times 10^{-3} \text{ g cm}^{-3}$ here. It is noteworthy
235 that the value of 2 is assigned to μ for both BR and LD schemes. Figure 2 compares the EN
236 scheme with the selected four schemes with a wide range of CWCs from 0.01 to 1.0 g m^{-3} . One
237 can see that all the schemes yield ATC rates of $\sim 10^{-9} \text{ g cm}^{-3} \text{ s}^{-1}$, although there are significant
238 discrepancies among the different schemes. For the KS scheme, the ATC of cloud water to rain
239 water does not start until the CWC exceeds the threshold q_0 (Eg. 1). In contrast, the other
240 schemes are allowable even given fair low CWCs.

241 Comparatively speaking, both KS and LD predicts larger ATC rate than the other ATC
242 schemes (the BR or KK scheme) for a given CWC. As for the former group, LD yields the
243 largest ATC rate with CWC below 0.6 g m^{-3} , while KS generates the largest ATC with CWC
244 over 0.6 g m^{-3} . Wood and Blossey (2005) argued that the ATC rate defined in LD would give
245 the total rate of mass coalescence among cloud droplets and is typically much larger than the
246 true ATC rate. With N_c fixed at 300 cm^{-3} , the BR scheme shows close ATC rates to those of KK.
247 Note that the KK scheme, originally developed for the Large Eddy Simulation (LES) model,
248 yields the lowest ATC rate, followed by the BR scheme. The EN scheme provides a similar
249 pattern to LD, but nearly half ATC rates of those are yielded by the latter. It should be



250 emphasized that ATC rates are fairly sensitive to N_c (Fig. 1), and a higher or lower N_c would
251 cause greatly changes.

252 **4 Simulations of an extreme rainfall event**

253 **4.1 Overview of the rainfall event**

254 An extreme rainfall event hit Guangzhou megacity in the early morning hours of 7 May
255 2017. Within 18 hours (during the period of 2000 BST 6 May to 1400 BST 7 May), there
256 were 12 rain gauge stations over 250 mm during the rainfall process. The spatial distribution of
257 the rainfall appears two heavy rainfall cores over Jiulong (JL) and Huashan (HS) regions (Fig.
258 3a). The event was featured by the heaviest rainfall in Guangzhou megacity over the past six
259 decades with the maximum total amount of 542 mm within 18 hours at JL station (Fig. 3a). It
260 also broke the record of 3-h accumulated rainfall amount with the value of 382 mm. Another
261 marked feature of this rainfall event was its extreme hourly rainfall rate of 184 mm h^{-1} , which
262 is the second highest over the, Guangdong Province, China. The hourly rainfall rate is
263 comparable to the highest value of 188 mm h^{-1} observed at Yangjiang station in Guangdong
264 Province on 23 June 2013.

265 **4.2 Model configuration and experiment settings**

266 This event was well simulated and investigated by Yin et al. (2020), focusing on the
267 effects of urbanization and orography. The WRF model configurations, and initial and
268 boundary conditions are the same as Yin et al. (2020) except for updating to the
269 WRF-ARW(v4.1.3) model (Skamarock et al., 2019) with several minor bugs fixed. For
270 convenience, an overview of the WRF model configures is presented here. The triple nested



271 domains have x, y dimensions of 313×202, 571×334, and 862×541 with grid sizes of 12, 4,
272 and 1.33 km, respectively. The WRF model physics schemes are configured with the
273 Thompson microphysics scheme ([Thompson et al., 2008](#)) with the modifications of ATC
274 parameterization, the rapid radiative transfer model (rrtm) ([Mlawer et al., 1997](#)) for both
275 shortwave and longwave radiative flux calculations, the Yonsei University (YSU) planetary
276 boundary layer (PBL) scheme ([Hong et al., 2006](#)), the MM5 Monin-Obukhov scheme for the
277 surface layer ([Janjić, 1994](#)), and the Noah-MP land-surface scheme ([Niu et al., 2011](#)). The Kain
278 cumulus parameterization scheme ([Kain, 2004](#)) is utilized for the outer two coarse resolution
279 domains, but being bypassed in the finest domain. All the three nested domains of the WRF
280 model are integrated for 18 hours, starting from 2000 BST 06 May 2017, with outputs at 6-min
281 intervals. The initial and outermost boundary conditions are interpolated from the National
282 Centers for Environmental Prediction (NCEP) Global Forecast System 0.25 degree re-analysis
283 data at 6-h intervals. In order to introduce realistically the UHI effects of the Guangzhou
284 metropolitan region, the Four-Dimension Data Assimilation (FDDA) functions are activated
285 ([Reen, 2016](#)) by performing both the surface observation nudging and the analysis nudging
286 from 2000 BST 6 to 0800 BST 7 May 2017. Please refer to Yin et al. ([2020](#)) for more details
287 about the model configuration.

288 As has been addressed above, it is convenient to a launch simulation with any of the above
289 listed ATC scheme alone. In total, two experiments were carried out with the EN and BR
290 schemes. It should be noted that the BR scheme was used originally in the Thompson scheme,
291 and the EN were newly coupled into the Thompson scheme in this work.



292 **5. Results**

293 **5.1 Spatial distribution of accumulated rainfall**

294 Figure 3 compares the spatial distribution of 18-h simulated total rainfall from the
295 simulations with the EN and BR schemes to the observed. Generally speaking, both the
296 schemes are able to capture main characteristics of the extreme rainfall event. One can see
297 that the simulated rainfall amount compares favorably to the observed both at HS and at JL,
298 although the JL storm has a 10-15 km eastward location shift. Yin et al. (2020) argued that the
299 location errors may be related to large-scale meteorological conditions. Comparatively
300 speaking, the EN and BR schemes performed better than others. The two centralized rainfall
301 cores over HS and JL were successfully captured by the EN and BR schemes, with the
302 simulated heaviest rainfall amount of 537 mm and 569 mm, respectively (Fig. 3b,c). As for
303 the EN scheme (Fig. 3b), the simulated 18-h total rainfall were 320 mm and 537 mm over HS
304 and JL, respectively, which was close to the observations of 341 mm and 542 mm (Fig. 3a).
305 Similarly, the BR scheme performed equivalently to the EN scheme, with the maximum
306 rainfall of 347 mm and 569 mm over Huashan and Jiulong regions, respectively (Fig. 3c).
307 Note that the simulated heaviest over Huashan region were comparative among each other. In
308 view of the results, we will compare the maximum hourly rainfall rates near JL from the
309 simulations of the EN and BR schemes to that of observed in the next sections. It should be
310 noted the results in the present study are a little better than (or equivalent to at least) those in
311 Yin et al. (2020) because of the update of the WRF version4.1.3 model with some
312 improvements in dynamical framework and bug fixes.



313 **5.2 Evolution of the simulated hourly rainfall**

314 Figure 4 shows the observed and simulated time series of hourly maximum rainfall rates
315 over the Jiulong region. The observed peak rainfall near JL occurred at 0600 BST 7 May with
316 the hourly rates of 184 mm hr^{-1} . However, the simulated peak rainfall from the EN scheme took
317 place at 0700 BST 7 May, which was about 1 h later than the observed, with the hourly rates of
318 151 mm hr^{-1} . As for the BR scheme, the simulated peak rainfall rate occurred two hours later,
319 with the value of 144 mm hr^{-1} . As a matter of fact, both EN and BR schemes under-predicted
320 the peak hourly rainfall rate near JL. It is worthy to note that the observed timings of initiating
321 and ending of the ER production episode, i.e., near 0300 and 1000 BST 7 May, respectively,
322 were reproduced successfully. However, the both simulated peak rate occurred later than the
323 observed due to the slower increases in rain-producing rates than the observed. More
324 specifically, the observed hourly rate increased from about 16 mm hr^{-1} to 184 mm hr^{-1} just in
325 one hour (i.e., from 0500 to 0600 BST). However, the simulated from the EN scheme increased
326 from 0.3 mm hr^{-1} at 0400 BST to about 79 mm hr^{-1} at 0600 BST, and then to 151 mm hr^{-1} at
327 0700 BST 7 May. As for the simulated with the BR scheme, it increased from 2 mm hr^{-1} at 0400
328 BST to about 104 mm hr^{-1} at 0700 BST, and then to 144 mm hr^{-1} at 0800 BST 7 May. One
329 unique feature of the observed was the rapid increase of hourly rainfall rate. The rainfall
330 produced by the EN scheme peaked within 2 h while the BR scheme peaked over a period of 4
331 h. Additionally, both the simulated rainfall rates decrease over a period of several hours.
332 Generally speaking, the EN scheme performed much closer to the observed, compared to that
333 of the BR scheme. Note that the longer heavy rainfall period from the BR scheme contributed
334 partially to the over-prediction of the 18-h accumulated rainfall (Fig. 3c).



335 **5.3 Evolutions of radar reflectivity**

336 In view of the performance of the accumulated rainfall and the maximum hourly rainfall
337 rates, we only compare the radar reflectivity from the simulations with the EN scheme to the
338 results of the BR scheme. Figure 5 exhibits the structures and evolutions of convective cells
339 over JL region by comparing the simulated composite radar reflectivity to the observed. The
340 first well-organized radar echo formed near 0000 BST over Huashan region (not shown), which
341 was located at the northern edge of a surface high- θ_e (equivalent potential temperature) tongue
342 with significant convergence. As the southeasterly flow moved slowly eastward and the cold
343 outflows resulted from previous convection, the Huashan storm dissipated while the storm
344 began to develop over Jiulong region, both in its size and in intensity (Fig. 5a). The storm
345 rapidly intensified during the period from 0430 to 0530 BST, with the peak reflectivity beyond
346 55 dBZ near the leading edge (Fig. 5a,b). The Jiulong storm moved fairly slowly, keeping more
347 or less quasi-stationary shortly after its formation (Fig. 5a-c). Both the quasi-stationary nature
348 and intense radar reflectivity explain the extreme rainfall production rate occurring at JL during
349 the 1-h period of 0500 - 0600 BST. Subsequently, the Jiulong storm weakened, but its
350 associated peak radar reflectivity still remained over 50 dBZ, which was consistent with the
351 continued generation of significant rainfall near JL until 0800 BST (Fig. 4).

352 It is obvious that the both the EN and BR schemes captured the development of the
353 Jiulong storm, with the main features that were similar to the observed, including
354 quasi-stationary nature, southeastward expansion, and concentrated strong radar reflectivity
355 during the extreme rainfall stage. Both simulations successfully generated a lower- θ_e pool with
356 a distinct outflow boundary interacting with the moist southeasterly flow near the ground. It



357 should be noted that the initiation and organization of the both simulated Jiulong storm were
358 about 1.7 h later than the observed, and it occurred at a location nearly 10-15 km kilometers to
359 the east of the observed one. Generally speaking, both simulations with the EN and BR
360 schemes produced extreme rainfall amounts close to those observed and their spatial
361 distributions agree well with observations.

362 In terms of the spatial distribution of radar reflectivity, similar patterns can be seen
363 between the EN and BR schemes in the early stage before 0712 UTC, while differences are
364 visible at the extreme rainfall stage (Fig. 5e,h). One can find that the Jiulong storm simulated
365 with the EN scheme (Fig. 5f) developed more rapidly than that from the BR scheme, almost 1
366 h earlier than the latter (Fig. 5i). This was consistent with the timing lag in the hourly extreme
367 rainfall production (Fig. 4). Clearly, ACT process has an important influence on convective
368 development of deep convection associated with the extreme rainfall producing within the
369 Jiulong storm, which will be explored in view of the cloud microphysical processes in the
370 next section.

371 **5.4 The Effects on Macro- and Micro-physical Processes**

372 The spatial distribution of hourly rainfall, and temporal-averaged surface temperature
373 and horizontal wind during the period from 0600 BST to 0700 BST from the simulations with
374 the EN and BR schemes are displayed in Fig. 6. As has been stated above, the total rainfall
375 show slight difference between EN and BR over Jiulong region (Fig. 3b,c). In view of the
376 spatial distribution of the maximum hourly rainfall (Fig. 6), the EN scheme generated larger
377 rainfall area and stronger rainfall rate than those of the BR scheme, although both scheme
378 produced similar spatial distribution patterns in rainfall area, and temporal-averaged surface



379 temperature and horizontal wind filed. The result was consistent with the idealized experiment
380 in Fig. 2. For a given CWC, the EN scheme had a larger ATC rate, compared to the BR
381 scheme, and the difference becomes obvious with the increasing of CWC. The ATC process
382 mostly occurred at lower levels, resulting in higher number concentration of small raindrops
383 ([Duan et al., 2020](#)). The higher number concentration of middle-size raindrop was favorable
384 for coalescence of large precipitation particles from the upper levels, which made the larger
385 contribution to the extreme rainfall rate (e.g., [Bao et al., 2019](#)). As a result, the EN scheme
386 produced larger rainfall than the BR scheme. The result was consistent with Fu and Lin
387 ([2019](#)). The temporal and spatial extent of the “vigorous rain formation region” where most of
388 the rain was produced. Those features can also be viewed from the vertical sections in Fig. 7.
389 One can see that the largest radar reflectivity reaches the ground, like a bell on the ground
390 (Fig. 7a). This unique feature was reported by Li et al. ([2020](#)) based on the observations from
391 the S-band dual-polarization radar at Guangzhou station, Guangdong Province, China. The
392 bell-shaped radar reflectivity was consistent with the episode of the extreme hourly rainfall.
393 The strong radar reflectivity mainly resulted from raindrops coalescence owing to the higher
394 number concentration raindrop in the lower levels ([Bao et al., 2020](#)). That is to say, collecting
395 rain water by collision-coalescence process at the lower levels helped creat the large rainfall
396 rate at the ground. As for the BR scheme (Fig. 7b), a middle-level radar reflectivity cores was
397 obvious above nearly 1 km up to 4 km, indicating that raindrops coalescence occurred
398 intensively between those levels and evaporation of raindrop was significant below 1 km. The
399 evaporation near above the surface was a considerable factor abating the surface rainfall rate.
400 In view of the vertical distribution of radar reflectivity, the EN scheme generated a



401 maritime-like convective storm, whereas the convective storm simulated by the BR scheme
402 was close to a continental-like convection. That is to say, the latter have a smaller number of
403 raindrops near the surface.

404 Both the EN and BR schemes provide tilted storms in view of vertical cross from south to
405 north through the extreme rainfall. During this episode, the updraft was dominant in the storm,
406 and very weak downdraft occurred in the lower levels at the back of the convective storm.
407 Besides, both EN and BR reproduced very close thermal patterns in terms of potential
408 temperature. Note that the EN scheme had a slightly weaker in updraft than that of the BR
409 scheme, although only make the modification in the ATC parameterization in the
410 microphysics scheme (Fig. 7a,b), suggesting that change in cloud microphysical processes can
411 lead to some variations in dynamical processes.

412 The difference between EN scheme and BR scheme in updraft can be also viewed from
413 the cumulative contoured frequency by altitude diagrams (CCFAD) given in Fig. 8. CCFAD
414 presents the percentage of horizontal grid points with vertical motion weaker than the abscissa
415 scaled value for a given height ([Yuter and Houze, 1995](#)). In this study, vertical speeds are
416 binned with intervals of 1 m s^{-1} based on the evelen model outputs with six-minute intervals
417 during the severe rainfall episode from 0600 BST to 0700 BST 7 May, 2017. Generally
418 speaking, the EN scheme shows similar CCFAD patterns to those of the BR scheme. However,
419 there are still various differences in the vertical motion. One can see there was a slight weaker
420 core but lower in the EN scheme simulation, compared to those of the BR scheme. During the
421 severe rainfall episode, the EN scheme produced the largest updraft nearly 15 m s^{-1} at 5 km
422 level, while that was about 16 m s^{-1} at 6 km level given by the BR scheme. On the contrast,



423 updrafts below 6 m s^{-1} occurred more frequently in EN than that in the BR scheme. Overall,
424 the EN scheme provided a larger updraft area but slight weaker in upward speed, compared to
425 those in BR scheme. This is why the EN scheme had a larger spatial distribution of rainfall
426 than that of the BR scheme (Fig. 6a,b). Note that both EN and BR schemes had a slight
427 difference in downdraft in vertical distribution and the downdraft was mainly located below 2
428 km, which were also visible in the vertical cross sections (Fig. 7a,b).

429 As has been noted above, both the EN and BR schemes produced very close dynamical
430 patterns except for updrafts. However, differences were remarkable in cloud microphysical
431 processes. Figure 9 compares the temporal evolution of hydrometeors between EN scheme
432 and BR scheme. One can see that the EN scheme (Fig. 9a-f) produced similar hydrometeors
433 patterns to those of the BR scheme (Fig.9g-i). Overall, graupel was dominant above the
434 melting layer, while rainwater was considerable below the melting layer. Previous studies
435 ([Franklin et al., 2005](#); [Krueger et al., 1995](#); [McCumber et al., 1991](#); [Yin et al., 2018](#)) proposed
436 that graupel was dominant in the tropical and subtropical clouds owing to plentiful water
437 vapor. Overall, the EN scheme mainly increased rainwater content and graupel, while only
438 slight differences in cloud water, cloud ice, snow, and water vapor, compared with those of
439 the BR scheme (Fig. 9m-r).

440 In terms of the difference in rainwater and graupel between the EN and the BR schemes
441 (Fig. 9m-r), we find that the ATC rate of the EN scheme played an important role in the
442 development of deep convection. Compared to the BR scheme, the higher ATC rate of the EN
443 scheme quickly produced more considerable number of small precipitation-sized drops within
444 updrafts in moderate- and lower-levels, and more of the small size raindrops were lofted by



445 the updrafts above the 0°C level and subsequently were fed for ice processes. Within this
446 graupel coexisted with more small supercooled rainwater region, stronger riming occurred
447 between ice particles and the small size rain drops. Consequently, more of the small
448 supercooled raindrops were converted into graupel by ice cloud microphysical process such as
449 riming, leading to a more rapid graupel production. At the same time (Fig. 9q), more
450 supercooled raindrops froze becoming more graupel embryos since bigger raindrops freeze at
451 warmer temperatures than smaller cloud droplets, and continue to grow by riming and/or
452 other processes. Consequently, graupel was increased at high altitude (above the 0°C) levels.
453 It is well known that bigger water drops freeze at warmer temperatures than small drops.
454 Therefore, partial the small raindrops froze into graupel and snow particles, which contributes
455 the increasement in graupel and snow. Generally, a graupel particle has a larger size than a
456 raindrop with a given mass. Therefore, the larger graupel particle can collect more particles as
457 they fall downward in the storm, which helped creat the surface heavy rainfall rate. One can
458 see that the graupel increased rapidly nearly 12 minutes after the appearance of increasing
459 supercooled rain (Fig. 9n). It should be noted we try to understand cloud mirophysical
460 processes in the extreme rainfall based on our knowledge at present, and thus a rigorous
461 validation is required by comparing hydrometeors sink and terms in a future study.

462 As the increased graupel passed by the melting level, they started to melt leading to
463 more raindrops. In view of the strong radar reflectivity near the surface in Fig. 7a, the
464 raindrops from upper levels grew rapidly by collecting raindrops in the lower levels. In this
465 way, the extreme rainfall rate was generated in such a more rapid and efficient approach,
466 compared those of the BR scheme. During this stage, the increased ATC rate was linked to



467 ice-phase processes and modified graupel fraction above the 0°C level. As has been
468 mentioned earlier, the increased ATC rate played a certain role in dynamical feedbacks, and
469 the degree of modulation of water vapor, cloud water, cloud ice, and snow by the increased
470 ATC rate was negligible. These findings indicate that increased ATC rate were important in
471 the extreme rainfall that involved ice-phase processes of graupel above the 0°C levels and
472 warm-rain processes of rain drop in the lower levels. To summarize, the higher ATC rate of
473 the EN scheme produced more small precipitation-sized drops, and some of the small size
474 raindrops were lofted by above the 0°C level. Consequently, more graupel were generated by
475 riming and freezing processes. The rapid production of graupel played significant roles in the
476 development of the extreme rainfall. Collision and coalescence processes between liquid
477 particles appeared to be the mechanism of radar reflectivity increment toward the surface
478 within the storm core region.

479 We proposed the influence mechanism of ATC rate on the extreme rainfall by comparing
480 the simulated results between the EN scheme and the BR scheme. However, there are still
481 some limitations to figure out the complete effects of the increasing ATC rate on
482 microphysical and dynamical processes at present because those processes are entangled with
483 complicated interactions. Therefore, a better choice is to separate the effects on each process
484 by conducting high-resolution simulations with a sophisticated model, such as the approach of
485 Grabowski (2014). Certainly, the best way is to perform offline testing based on in-situ
486 observations, as was done by Wood (2005). Keeping those issues in our mind, further work is
487 needed to address this question.



488 **6 Conclusions and Discussion**

489 In this study, we designed an ensemble (EN) approach to improving ATC process
490 description in the cloud microphysics schemes. One unique feature of the EN approach is that
491 the ATC rate is a mean value based on the calculations from the several widely used ATC
492 schemes. Similar to ensemble prediction, this approach is aimed to improve the representation
493 of the ATC rate in case it has been treated by using an ATC scheme alone in the cloud
494 microphysics schemes. At present, the four widely used ATC schemes are selected, including
495 Kessler ([1969](#)) scheme, Berry and Reinhardt ([1974](#)) scheme, Khairoutdinov and Kogan ([2000](#))
496 scheme, and Liu et al. ([2006](#)) scheme. In the EN scheme, each scheme is assigned a weight (Eq.
497 7) in order to modulate the importance of them. Certainly, the EN scheme is easily reduced
498 into any single scheme by setting all w_{xx} values of 0 except for one of them. It is also convenient
499 to reduce the effect of a scheme by giving a small value of w_{xx} , even remove the effect of a
500 scheme by assigning a value of weight to 0. Under this framework, the ATC rates from the EN
501 scheme are compared to those from each of the several commonly used schemes by ideal
502 experiments, and a series of simulations are carried out for a urban-induced extreme rainfall
503 event over Southern China by using the EN, KE, BR, KK, and LD schemes which have been
504 coupled into the Thompson scheme in the WRF model ([Thompson et al., 2008](#)) in this work.
505 The results show that the EN scheme provides better simulations, compared to those from any
506 single ATC scheme used alone.

507 In this study, the ensemble approach has been employed to represent the ATC process in
508 the Thompson cloud microphysics scheme, which shows some advantages for simulation of



509 the extreme rainfall event, occurred on 7 May 2017 over southern China. It is important to
510 acknowledge that the conclusions are drawn from just one case study, and have not been
511 validated under a wider range of conditions over the world. In the forthcoming studies,
512 systematic assessment of more heavy rainfall events is planned to better understand the
513 performance of the EN scheme. It should be noted that there are still some limitation to the
514 EN scheme in the present study. Although a large number of ATC schemes are available, most
515 among them are not employed as ensemble member. For example, the Franklin scheme
516 ([Franklin, 2008](#)) took the effect of turbulence on the ATC process into account, which plays
517 important role in precipitation development ([Chandrakar et al., 2018](#); [Seifert et al., 2010](#)).
518 Furthermore, equal weights were used in the present study for convenience. In other words, the
519 selected schemes have the same effect on the ATC rate. Moreover, only conventional
520 verifications were carried out, and the dependency of the performance of the ATC schemes on
521 model resolution was not considered in this study. A further examination with new approaches
522 ([e.g., Wood, 2005](#); [Grabowski, 2014](#)) might provide important insights in the near future.

523 It is worth emphasizing that we focus our attention on the ATC from cloud water into
524 rainwater at present. Certainly, any source/sink term in a cloud microphysics scheme can be
525 dealt with the same method. Since developing a “unified” cloud scheme appears to be a
526 significant part of weather and climate model development in the coming years ([Randall et al.,](#)
527 [2019](#)), the EN approach may be a practicable way to reduce the potential uncertainty in cloud
528 and precipitation physical process, which will contribute to more accurate numerical model
529 development.

530



531 **Code and data availability:** The source code of the Weather Research and Forecasting model
532 (WRF v4.1.3) is available at <https://github.com/wrf-model/WRF/releases> (last access: July
533 2021). Modified WRF model codes and initial and boundary data used for the simulations are
534 available on Zenodo (<https://doi.org/10.5281/zenodo.5052639>). The National Centers for
535 Environmental Prediction (NCEP) Global Forecast System 0.25 degree re-analysis data at 6-h
536 intervals used for the initial and boundary conditions for the specific analysed period can be
537 downloaded at <https://rda.ucar.edu/datasets/ds083.2/>.

538 **Competing interests:** The author declares no competing interests.

539 **Author contributions.** J. Yin developed the weighted ensemble scheme and coupled the
540 scheme into the WRF model, with contributions from X. Liang. J. Yin tested and verified the
541 scheme with contributions from X. Liang, H. Wang, and H Xue. J. Yin wrote the manuscript,
542 and all the authors continuously discussed the results and contributed to the improvement of
543 the paper text.

544 **Acknowledgements:** This study is jointly supported by the National Natural Science
545 Foundation of China (42075083), National Key Research and Development Program of China
546 (2018YFC1507404 and 2017YFC1501806), and Development Foundation of Chinese
547 Academy of Meteorological Sciences (2019KJ026). The authors also acknowledge the use of
548 the NCAR Command Language (NCL) in the analysis of some of the WRF Model output and
549 the preparation of figures.

550



551 **References:**

- 552 Bao, X., Wu, L., Tang, B., Ma, L., Wu, D., Tang, J., Chen, H., and Wu, L.: Variable
553 Raindrop Size Distributions in Different Rainbands Associated With Typhoon
554 Fitow (2013), *J. Geophys. Res.: Atmos.*, 124, 12262-12281,
555 <https://doi.org/10.1029/2019JD030268>, 2019.
- 556 Bao, X., Wu, L., Zhang, S., Li, Q., Lin, L., Zhao, B., Wu, D., Xia, W., and Xu, B.:
557 Distinct Raindrop Size Distributions of Convective Inner- and Outer-Rainband
558 Rain in Typhoon Maria (2018), *J. Geophys. Res.: Atmos.*, 125, e2020JD032482,
559 <https://doi.org/10.1029/2020JD032482>, 2020.
- 560 Beheng, K. D.: A parameterization of warm cloud microphysical conversion processes,
561 *Atmos. Res.*, 33, 193-206, [https://doi.org/10.1016/0169-8095\(94\)90020-5](https://doi.org/10.1016/0169-8095(94)90020-5), 1994.
- 562 Berry, E. X.: Modification of the warm rain process. Preprints, First National Conf. on
563 Weather Modification, Albany, NY, Amer. Meteor. Soc., 81–88, 1968.
- 564 Berry, E. X. and Reinhardt, R. L.: An Analysis of Cloud Drop Growth by Collection
565 Part II. Single Initial Distributions, *J. Atmos. Sci.*, 31, 1825-1831,
566 [https://doi.org/10.1175/1520-0469\(1974\)031<1825:aaocdg>2.0.co;2](https://doi.org/10.1175/1520-0469(1974)031<1825:aaocdg>2.0.co;2), 1974.
- 567 Caro, D., Wobrock, W., Flossmann, A. I., and Chaumerliac, N.: A two-moment
568 parameterization of aerosol nucleation and impaction scavenging for a warm
569 cloud microphysics: description and results from a two-dimensional simulation,
570 *Atmos. Res.*, 70, 171-208, <http://dx.doi.org/10.1016/j.atmosres.2004.01.002>,
571 2004.
- 572 Chandrakar, K. K., Cantrell, W., and Shaw, R. A.: Influence of Turbulent Fluctuations
573 on Cloud Droplet Size Dispersion and Aerosol Indirect Effects, *J. Atmos. Sci.*, 75,
574 3191-3209, <https://doi.org/10.1175/JAS-D-18-0006.1>, 2018.
- 575 Chen, S.-H. and Sun, W.-Y.: A One-dimensional Time Dependent Cloud Model, *J.*
576 *Meteor. Soc. Japan*, 80, 99-118, <https://doi.org/10.2151/jmsj.80.99>, 2002.
- 577 Cotton, W. R.: Numerical Simulation of Precipitation Development in Supercooled
578 Cumuli—Part I, *Mon. Wea. Rev.*, 100, 757-763,
579 [https://doi.org/10.1175/1520-0493\(1972\)100<0757:NSOPDI>2.3.CO;2](https://doi.org/10.1175/1520-0493(1972)100<0757:NSOPDI>2.3.CO;2), 1972.
- 580 Doswell, C. A., III: Severe Convective Storms—An Overview, *Meteor. Monogr.*, 50,
581 1-26, <https://doi.org/10.1175/0065-9401-28.50.1>, 2001.
- 582 Duan, Y., Wan, Q., Huang, J., Zhao, K., Yu, H., Wang, Y., Zhao, D., Feng, J., Tang, J.,
583 Chen, P., Lu, X., Wang, Y., Liang, J., Wu, L., Cui, X., Xu, J., and Chan, P.-W.:



- 584 Landfalling Tropical Cyclone Research Project (LTCRP) in China, *Bull. Amer.*
585 *Meteor. Soc.*, 100, ES447-ES472, <https://doi.org/10.1175/BAMS-D-18-0241.1>,
586 2020.
- 587 Dudhia, J.: Numerical Study of Convection Observed during the Winter Monsoon
588 Experiment Using a Mesoscale Two-Dimensional Model, *J. Atmos. Sci.*, 46,
589 3077-3107,
590 [https://doi.org/10.1175/1520-0469\(1989\)046<3077:NSOCOD>2.0.CO;2](https://doi.org/10.1175/1520-0469(1989)046<3077:NSOCOD>2.0.CO;2), 1989.
- 591 Falk, N. M., Igel, A. L., and Igel, M. R.: The relative impact of ice fall speeds and
592 microphysics parameterization complexity on supercell evolution, *Mon. Wea.*
593 *Rev.*, 147, 2403-2415, <https://doi.org/10.1175/MWR-D-18-0417.1>, 2019.
- 594 FlatøY, F.: Comparison of two parameterization schemes for cloud and precipitation
595 processes, *Tellus A: Dyn. Meteorol. Ocean.*, 44, 41-53,
596 <https://doi.org/10.3402/tellusa.v44i1.14942>, 1992.
- 597 Franklin, C. N.: A Warm Rain Microphysics Parameterization that Includes the Effect
598 of Turbulence, *J. Atmos. Sci.*, 65, 1795-1816,
599 <https://doi.org/10.1175/2007JAS2556.1>, 2008.
- 600 Franklin, C. N., Holland, G. J., and May, P. T.: Sensitivity of Tropical Cyclone
601 Rainbands to Ice-Phase Microphysics, *Mon. Wea. Rev.*, 133, 2473-2493,
602 <https://doi.org/10.1175/MWR2989.1>, 2005.
- 603 Freeman, S. W., Igel, A. L., and van den Heever, S. C.: Relative sensitivities of
604 simulated rainfall to fixed shape parameters and collection efficiencies, *Quart. J.*
605 *Royal Meteor. Soc.*, 145, 2181-2201, <https://doi.org/10.1002/qj.3550>, 2019.
- 606 Fu, H. and Lin, Y.: A Kinematic Model for Understanding Rain Formation Efficiency
607 of a Convective Cell, *J. Adv. Model. Earth Sy.*, 11, 4395-4422,
608 <https://doi.org/10.1029/2019MS001707>, 2019.
- 609 Ghosh, S. and Jonas, P. R.: On the application of the classic Kessler and Berry schemes
610 in Large Eddy Simulation models with a particular emphasis on cloud
611 autoconversion, the onset time of precipitation and droplet evaporation, *Ann.*
612 *Geophys.*, 16, 628-637, <https://doi.org/10.1007/s00585-998-0628-2>, 1999.
- 613 Gilmore, M. S. and Straka, J. M.: The Berry and Reinhardt Autoconversion
614 Parameterization: A Digest, *J. Appl. Meteor. Clim.*, 47, 375-396,
615 <https://doi.org/10.1175/2007JAMC1573.1>, 2008.
- 616 Gilmore, M. S., Straka, J. M., and Rasmussen, E. N.: Precipitation uncertainty due to
617 variations in precipitation particle parameters within a simple microphysics



- 618 scheme, *Mon. Wea. Rev.*, 132, 2610-2627, <https://doi.org/10.1175/MWR2810.1>,
619 2004.
- 620 Grabowski, W. W., Wu, X., and Moncrieff, M. W.: Cloud Resolving Modeling of
621 Tropical Cloud Systems during Phase III of GATE. Part III: Effects of Cloud
622 Microphysics, *J. Atmos. Sci.*, 56, 2384-2402,
623 [https://doi.org/10.1175/1520-0469\(1999\)056<2384:CRMOTC>2.0.CO;2](https://doi.org/10.1175/1520-0469(1999)056<2384:CRMOTC>2.0.CO;2), 1999.
- 624 Grabowski, W. W.: Extracting Microphysical Impacts in Large-Eddy Simulations of
625 Shallow Convection, *J. Atmos. Sci.*, 71, 4493-4499,
626 <https://doi.org/10.1175/JAS-D-14-0231.1>, 2014.
- 627 Grabowski, W. W., Morrison, H., Shima, S.-I., Abade, G. C., Dziekan, P., and
628 Pawlowska, H.: Modeling of Cloud Microphysics: Can We Do Better?, *Bull.*
629 *Amer. Meteor. Soc.*, 100, 655-672, <https://doi.org/10.1175/BAMS-D-18-0005.1>,
630 2019.
- 631 Griffin, B. M. and Larson, V. E.: Analytic upscaling of a local microphysics scheme.
632 Part II: Simulations, *Quart. J. Royal Meteor. Soc.*, 139, 58-69,
633 <https://doi.org/10.1002/qj.1966>, 2013.
- 634 Hong, S.-Y., Noh, Y., and Dudhia, J.: A new vertical diffusion package with an explicit
635 treatment of entrainment processes, *Mon. Wea. Rev.*, 134, 2318-2341,
636 <https://doi.org/10.1175/MWR3199.1>, 2006.
- 637 Houghton, J. T., Ding, Y. H., Griggs, D. J., Noguera, M., Linden, P. J. v. d., Dai, X.,
638 K. Maskell, and Johnson, C. A. (Eds.): *Climate Change 2001: The Scientific Basis*,
639 Cambridge University Press, Cambridge, 49 pp., 2001.
- 640 Hsieh, W. C., Jonsson, H., Wang, L. P., Buzorius, G., Flagan, R. C., Seinfeld, J. H., and
641 Nenes, A.: On the representation of droplet coalescence and autoconversion:
642 Evaluation using ambient cloud droplet size distributions, *J. Geophys. Res.: Atmos.*,
643 114, <https://doi.org/10.1029/2008JD010502>, 2009.
- 644 Iacobellis, S. F. and Somerville, R. C. J.: Evaluating parameterizations of the
645 autoconversion process using a single-column model and Atmospheric Radiation
646 Measurement Program measurements, *J. Geophys. Res.: Atmos.*, 111, n/a-n/a,
647 <https://doi.org/10.1029/2005jd006296>, 2006.
- 648 Janjić, Z. I.: The step-mountain eta coordinate model: further developments of the
649 convection, viscous sublayer, and turbulence closure schemes, *Mon. Wea. Rev.*,
650 122, 927-945,
651 [https://doi.org/10.1175/1520-0493\(1994\)122<0927:TSMECM>2.0.CO;2](https://doi.org/10.1175/1520-0493(1994)122<0927:TSMECM>2.0.CO;2), 1994.



- 652 Jing, X., Suzuki, K., and Michibata, T.: The Key Role of Warm Rain Parameterization
653 in Determining the Aerosol Indirect Effect in a Global Climate Model, *J. Climate*,
654 32, 4409-4430, <https://doi.org/10.1175/JCLI-D-18-0789.1>, 2019.
- 655 Kain, J. S.: The Kain–Fritsch Convective Parameterization: An Update, *J. Appl.*
656 *Meteor.*, 43, 170-181,
657 [https://doi.org/10.1175/1520-0450\(2004\)043<0170:TKCPAU>2.0.CO;2](https://doi.org/10.1175/1520-0450(2004)043<0170:TKCPAU>2.0.CO;2), 2004.
- 658 Kessler, E.: On the Distribution and Continuity of Water Substance in Atmospheric
659 Circulations, *Circulations. Meteor. Monogr.*, 10. American Meteorological
660 Society, Boston 1969.
- 661 Khain, A. P., Beheng, K. D., Heymsfield, A., Korolev, A., Krichak, S. O., Levin, Z.,
662 Pinsky, M., Phillips, V., Prabhakaran, T., Teller, A., van den Heever, S. C., and
663 Yano, J. I.: Representation of microphysical processes in cloud-resolving models:
664 Spectral (bin) microphysics versus bulk parameterization, *Rev. Geophys.*, 53,
665 2014RG000468, <https://doi.org/10.1002/2014RG000468>, 2015.
- 666 Khairoutdinov, M. and Kogan, Y.: A New Cloud Physics Parameterization in a
667 Large-Eddy Simulation Model of Marine Stratocumulus, *Mon. Wea. Rev.*, 128,
668 229-243, [https://doi.org/10.1175/1520-0493\(2000\)128<0229:ancppi>2.0.co;2](https://doi.org/10.1175/1520-0493(2000)128<0229:ancppi>2.0.co;2),
669 2000.
- 670 Kogan, Y. and Ovchinnikov, M.: Formulation of Autoconversion and Drop Spectra
671 Shape in Shallow Cumulus Clouds, *J. Atmos. Sci.*, 77, 711-722,
672 <https://doi.org/10.1175/JAS-D-19-0134.1>, 2019.
- 673 Kong, F. and Yau, M. K.: An explicit approach to microphysics in MC2, *Atmos.-Ocean*,
674 35, 257-291, <https://doi.org/10.1080/07055900.1997.9649594>, 1997.
- 675 Krueger, S. K., Fu, Q., Liou, K. N., and Chin, H.-N. S.: Improvements of an Ice-Phase
676 Microphysics Parameterization for Use in Numerical Simulations of Tropical
677 Convection, *J. Appl. Meteor.*, 34, 281-287,
678 <https://doi.org/10.1175/1520-0450-34.1.281>, 1995.
- 679 Lee, H. and Baik, J.-J.: A physically based autoconversion parameterization, *J. Atmos.*
680 *Sci.*, 74, 1599-1616, <https://doi.org/10.1175/JAS-D-16-0207.1>, 2017.
- 681 Lei, H., Guo, J., Chen, D., and Yang, J.: Systematic Bias in the Prediction of
682 Warm-Rain Hydrometeors in the WDM6 Microphysics Scheme and
683 Modifications, *J. Geophys. Res.: Atmos.*, 125, e2019JD030756,
684 <https://doi.org/10.1029/2019JD030756>, 2020.
- 685 Lewis, J. M.: Roots of Ensemble Forecasting, *Mon. Wea. Rev.*, 133, 1865-1885,



- 686 <https://doi.org/10.1175/MWR2949.1>, 2005.
- 687 Li, M., Luo, Y., Zhang, D.-L., Chen, M., Wu, C., Yin, J., and Ma, R.: Analysis of a
688 record-breaking rainfall event associated with a monsoon coastal megacity of
689 south China using multi-source data, *IEEE Trans. Geosci. Remote Sens.*,
690 <https://doi.org/10.1109/TGRS.2020.3029831>, 2020.
- 691 Li, X.-Y., Brandenburg, A., Svensson, G., Haugen, N. E. L., Mehlig, B., and
692 Rogachevskii, I.: Condensational and Collisional Growth of Cloud Droplets in a
693 Turbulent Environment, *J. Atmos. Sci.*, 77, 337-353,
694 <https://doi.org/10.1175/JAS-D-19-0107.1>, 2019.
- 695 Lin, B., Zhang, J., and Lohmann, U.: A New Statistically based Autoconversion rate
696 Parameterization for use in Large-Scale Models, *J. Geophys. Res. : Atmos.*, 107,
697 <https://doi.org/10.1029/2001JD001484>, 2002.
- 698 Liu, Y. and Daum, P. H.: Parameterization of the Autoconversion Process.Part I:
699 Analytical Formulation of the Kessler-Type Parameterizations, *J. Atmos. Sci.*, 61,
700 1539-1548,
701 [https://doi.org/10.1175/1520-0469\(2004\)061<1539:POTAPI>2.0.CO;2](https://doi.org/10.1175/1520-0469(2004)061<1539:POTAPI>2.0.CO;2), 2004.
- 702 Liu, Y., Daum, P. H., McGraw, R., and Wood, R.: Parameterization of the
703 Autoconversion Process. Part II: Generalization of Sundqvist-Type
704 Parameterizations, *J. Atmos. Sci.*, 63, 1103-1109,
705 <https://doi.org/10.1175/jas3675.1>, 2006.
- 706 Manton, M. J. and Cotton, W. R.: Parameterization of the Atmospheric Surface Layer, *J.*
707 *Atmos. Sci.*, 34, 331-334,
708 [https://doi.org/10.1175/1520-0469\(1977\)034<0331:POTASL>2.0.CO;2](https://doi.org/10.1175/1520-0469(1977)034<0331:POTASL>2.0.CO;2), 1977a.
- 709 Manton, M. I. and Cotton, W. R.: Formulation of Approximate Equations for Modeling
710 Moist Deep Convection on the Mesoscale. *Atmospheric Science Paper 266*,
711 Colorado State University, 62 pp, 1977b.
- 712 McCumber, M., Tao, W.-K., Simpson, J., Penc, R., and Soong, S.-T.: Comparison of
713 Ice-Phase Microphysical Parameterization Schemes Using Numerical Simulations
714 of Tropical Convection, *J. Appl. Meteor.*, 30, 985-1004,
715 <https://doi.org/10.1175/1520-0450-30.7.985>, 1991.
- 716 Michibata, T. and Takemura, T.: Evaluation of autoconversion schemes in a single
717 model framework with satellite observations, *J. Geophys. Res.: Atmos.*, 120,
718 9570-9590, <https://doi.org/10.1002/2015JD023818>, 2015.
- 719 Mlawer, E. J., Taubman, S. J., Brown, P. D., Iacono, M. J., and Clough, S. A.: Radiative



- 720 transfer for inhomogeneous atmospheres: RRTM, a validated correlated-k model
721 for the longwave, *J. Geophys. Res.: Atmos.*, 102, 16663-16682,
722 <https://doi.org/10.1029/97JD00237>, 1997.
- 723 Morrison, H., Thompson, G., and Tatarskii, V.: Impact of Cloud Microphysics on the
724 Development of Trailing Stratiform Precipitation in a Simulated Squall Line :
725 Comparison of One-and Two-Moment Schemes, *Mon. Wea. Rev.*, 137, 991-1007,
726 <https://doi.org/10.1175/2008MWR2556.1>, 2009.
- 727 Morrison, H., van Lier-Walqui, M., Fridlind, A. M., Grabowski, W. W., Harrington, J.
728 Y., Hoose, C., Korolev, A., Kumjian, M. R., Milbrandt, J. A., Pawlowska, H.,
729 Posselt, D. J., Prat, O. P., Reimel, K. J., Shima, S.-I., van Diedenhoven, B., and
730 Xue, L.: Confronting the Challenge of Modeling Cloud and Precipitation
731 Microphysics, *J. Adv. Model. Earth Sy.*, 12, e2019MS001689,
732 <https://doi.org/10.1029/2019MS001689>, 2020.
- 733 Naeger, A. R., Colle, B. A., Zhou, N., and Molthan, A.: Evaluating Warm and Cold
734 Rain Processes in Cloud Microphysical Schemes Using OLYMPEX Field
735 Measurements, *Mon. Wea. Rev.*, 148, 2163-2190,
736 <https://doi.org/10.1175/MWR-D-19-0092.1>, 2020.
- 737 Niu, G.-Y., Yang, Z.-L., Mitchell, K. E., Chen, F., Ek, M. B., Barlage, M., Kumar, A.,
738 Manning, K., Niyogi, D., Rosero, E., Tewari, M., and Xia, Y.: The community
739 Noah land surface model with multiparameterization options (Noah-MP): 1.
740 Model description and evaluation with local-scale measurements, *J. Geophys.*
741 *Res.: Atmos.*, 116, D12109, <https://doi.org/10.1029/2010JD015139>, 2011.
- 742 Onishi, R., Matsuda, K., and Takahashi, K.: Lagrangian Tracking Simulation of Droplet
743 Growth in Turbulence–Turbulence Enhancement of Autoconversion Rate*, *J.*
744 *Atmos. Sci.*, 72, 2591-2607, <https://doi.org/10.1175/JAS-D-14-0292.1>, 2015.
- 745 Posselt, D. J., He, F., Bukowski, J., and Reid, J. S.: On the Relative Sensitivity of a
746 Tropical Deep Convective Storm to Changes in Environment and Cloud
747 Microphysical Parameters, *J. Atmos. Sci.*, 76, 1163-1185,
748 <https://doi.org/10.1175/JAS-D-18-0181.1>, 2019.
- 749 Randall, D. A., Bitz, C. M., Danabasoglu, G., Denning, A. S., Gent, P. R., Gettelman,
750 A., Griffies, S. M., Lynch, P., Morrison, H., Pincus, R., and Thuburn, J.: 100 Years
751 of Earth System Model Development, *Meteor. Monogr.*, 59, 12.11-12.66,
752 <https://doi.org/10.1175/AMSMONOGRAPHS-D-18-0018.1>, 2019.
- 753 Reen, B.: A brief guide to observation nudging in WRF,



- 754 <https://www2.mmm.ucar.edu/wrf/users/docs/ObsNudgingGuide.pdf>, 2016.
- 755 Reisner, J., Rasmussen, R. M., and Bruintjes, R. T.: Explicit forecasting of supercooled
756 liquid water in winter storms using the MM5 mesoscale model, *Quart. J. Roy.
757 Meteor. Soc.*, 124, 1071-1107, <https://doi.org/10.1002/qj.49712454804> 1998.
- 758 Rutledge, S. A. and Hobbs, P. V.: The Mesoscale and Microscale Structure and
759 Organization of Clouds and Precipitation in Midlatitude Cyclones. XII: A
760 Diagnostic Modeling Study of Precipitation Development in Narrow Cold-Frontal
761 Rainbands, *J. Atmos. Sci.*, 41, 2949-2972,
762 [https://doi.org/10.1175/1520-0469\(1984\)041<2949:TMAMSA>2.0.CO;2](https://doi.org/10.1175/1520-0469(1984)041<2949:TMAMSA>2.0.CO;2), 1984.
- 763 Schultz, P.: An Explicit Cloud Physics Parameterization for Operational Numerical
764 Weather Prediction, *Mon. Wea. Rev.*, 123, 3331-3343,
765 [https://doi.org/10.1175/1520-0493\(1995\)123<3331:AECPPF>2.0.CO;2](https://doi.org/10.1175/1520-0493(1995)123<3331:AECPPF>2.0.CO;2), 1995.
- 766 Seifert, A. and Beheng, K. D.: A double-moment parameterization for simulating
767 autoconversion, accretion and selfcollection, *Atmos. Res.*, 59-60, 265-281,
768 [https://doi.org/10.1016/S0169-8095\(01\)00126-0](https://doi.org/10.1016/S0169-8095(01)00126-0), 2001.
- 769 Seifert, A., Nuijens, L., and Stevens, B.: Turbulence effects on warm-rain
770 autoconversion in precipitating shallow convection, *Quart. J. Royal Meteor. Soc.*,
771 136, 1753-1762, <https://doi.org/10.1002/qj.684>, 2010.
- 772 Silverman, B. A. and Glass, M.: A Numerical Simulation of Warm Cumulus Clouds:
773 Part I. Parameterized vs Non-Parameterized Microphysics, *J. Atmos. Sci.*, 30,
774 1620-1637,
775 [https://doi.org/10.1175/1520-0469\(1973\)030<1620:ANSOWC>2.0.CO;2](https://doi.org/10.1175/1520-0469(1973)030<1620:ANSOWC>2.0.CO;2), 1973.
- 776 Simpson, j. and Wiggert, v.: Models of precipitating cumulus towers, *Mon. Wea. Rev.*,
777 97, 471-489,
778 [https://doi.org/10.1175/1520-0493\(1969\)097<0471:MOPCT>2.3.CO;2](https://doi.org/10.1175/1520-0493(1969)097<0471:MOPCT>2.3.CO;2), 1969.
- 779 Skamarock, W. C., Klemp, J. B., Duda, M. G., Fowler, L. D., Park, S.-H., and Ringler, T.
780 D.: A Multiscale Nonhydrostatic Atmospheric Model Using Centroidal Voronoi
781 Tessellations and C-Grid Staggering, *Mon. Wea. Rev.*, 140, 3090-3105,
782 <https://doi.org/10.1175/MWR-D-11-00215.1>, 2012.
- 783 Skamarock, W. C., Klemp, J. B., Dudhia, J., Gill, D. O., Liu, Z., Berner, J., Wang, W.,
784 Powers, J. G., Duda, M. G., Barker, D. M., and Huang, X.-Y.: A Description of the
785 Advanced Research WRF Version 4. NCAR Tech. Note NCAR/TN-556+STR,
786 145 pp, <https://doi.org/10.5065/1dfh-6p97>, 2019.
- 787 Sundqvist, H., Berge, E., and Kristjánsson, J. E.: Condensation and Cloud



- 788 Parameterization Studies with a Mesoscale Numerical Weather Prediction Model,
789 Mon. Wea. Rev., 117, 1641-1657,
790 [https://doi.org/10.1175/1520-0493\(1989\)117<1641:cacpsw>2.0.co;2](https://doi.org/10.1175/1520-0493(1989)117<1641:cacpsw>2.0.co;2), 1989.
- 791 Tao, W.-K. and Simpson, J.: Goddard Cumulus Ensemble Model. Part I: Model
792 Description, Terr. Atmos. Oceanic Sci., 4, 35-72,
793 [https://doi.org/10.3319/TAO.1993.4.1.35\(A\)](https://doi.org/10.3319/TAO.1993.4.1.35(A)), 1993.
- 794 Tapiador, F. J., Sánchez, J.-L., and García-Ortega, E.: Empirical values and
795 assumptions in the microphysics of numerical models, Atmos. Res., 215, 214-238,
796 <https://doi.org/10.1016/j.atmosres.2018.09.010>, 2019.
- 797 Thompson, G., Rasmussen, R. M., and Manning, K.: Explicit Forecasts of Winter
798 Precipitation Using an Improved Bulk Microphysics Scheme. Part I: Description
799 and Sensitivity Analysis, Mon. Wea. Rev., 132, 519-542,
800 [https://doi.org/10.1175/1520-0493\(2004\)132<0519:EFOWPU>2.0.CO;2](https://doi.org/10.1175/1520-0493(2004)132<0519:EFOWPU>2.0.CO;2), 2004.
- 801 Thompson, G., Field, P. R., Rasmussen, R. M., and Hall, W. D.: Explicit Forecasts of
802 Winter Precipitation Using an Improved Bulk Microphysics Scheme. Part II:
803 Implementation of a New Snow Parameterization, Mon. Wea. Rev., 136,
804 5095-5115, <https://doi.org/10.1175/2008MWR2387.1>, 2008.
- 805 Wellmann, C., Barrett, A. I., Johnson, J. S., Kunz, M., Vogel, B., Carslaw, K. S., and
806 Hoese, C.: Comparing the impact of environmental conditions and microphysics
807 on the forecast uncertainty of deep convective clouds and hail, Atmos. Chem.
808 Phys., 20, 2201-2219, <https://doi.org/10.5194/acp-20-2201-2020>, 2020.
- 809 White, B., Gryspeerdt, E., Stier, P., Morrison, H., Thompson, G., and Kipling, Z.:
810 Uncertainty from the choice of microphysics scheme in convection-permitting
811 models significantly exceeds aerosol effects, Atmos. Chem. Phys., 17,
812 12145-12175, <https://doi.org/10.5194/acp-17-12145-2017>, 2017.
- 813 Wood, R.: Drizzle in Stratiform Boundary Layer Clouds. Part II: Microphysical
814 Aspects, J. Atmos. Sci., 62, 3034-3050, <https://doi.org/10.1175/JAS3530.1>, 2005.
- 815 Wood, R. and Blossey, P. N.: Comments on “Parameterization of the Autoconversion
816 Process. Part I: Analytical Formulation of the Kessler-Type Parameterizations”, J.
817 Atmos. Sci., 62, 3003-3006, <https://doi.org/10.1175/jas3524.1>, 2005.
- 818 Wood, R., Field, P. R., and Cotton, W. R.: Autoconversion rate bias in stratiform
819 boundary layer cloud parameterizations, Atmos. Res., 65, 109-128,
820 [http://dx.doi.org/10.1016/S0169-8095\(02\)00071-6](http://dx.doi.org/10.1016/S0169-8095(02)00071-6), 2002.
- 821 Xiao, H., Yin, Y., Zhao, P., Wan, Q., and Liu, X.: Effect of Aerosol Particles on

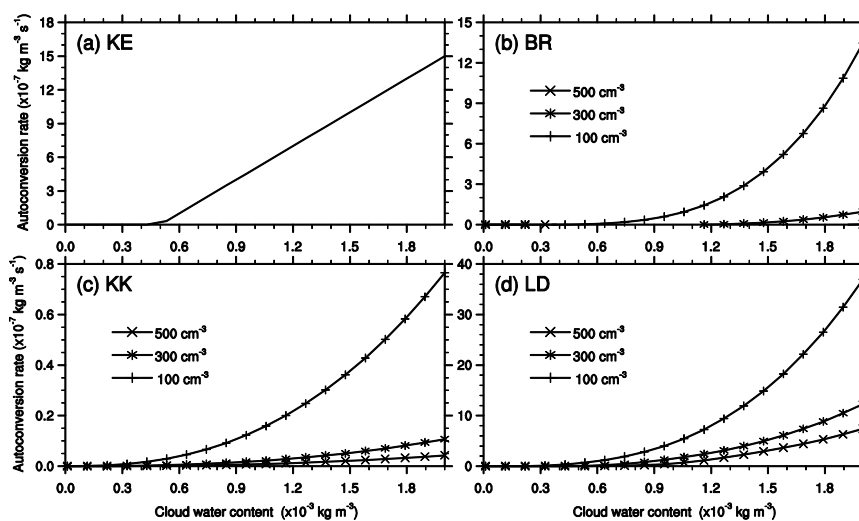


- 822 Orographic Clouds: Sensitivity to Autoconversion Schemes, *Advances in*
823 *Atmospheric Sciences*, 37, 229-238, <https://doi.org/10.1007/s00376-019-9037-6>,
824 2020.
- 825 Yin, J.-F., Wang, D.-H., Liang, Z.-M., Liu, C.-J., Zhai, G.-Q., and Wang, H.: Numerical
826 Study of the Role of Microphysical Latent Heating and Surface Heat Fluxes in a
827 Severe Precipitation Event in the Warm Sector over Southern China, *Asia-Pacific*
828 *J. Atmos. Sci.*, 54, 77-90, <https://doi.org/10.1007/s13143-017-0061-0>, 2018.
- 829 Yin, J., Wang, D., and Zhai, G.: An attempt to improve Kessler-type parameterization
830 of warm cloud microphysical conversion processes using CloudSat observations, *J.*
831 *Meteorol. Res.*, 29, 82-92, <https://doi.org/10.1007/s13351-015-4091-1>, 2015.
- 832 Yin, J., Zhang, D.-L., Luo, Y., and Ma, R.: On the Extreme Rainfall Event of 7 May
833 2017 Over the Coastal City of Guangzhou. Part I: Impacts of Urbanization and
834 Orography, *Mon. Wea. Rev.*, <https://doi.org/10.1175/MWR-D-19-0212.1>, 2020.
- 835 Yuter, S. E. and Houze, R. A.: Three-Dimensional Kinematic and Microphysical
836 Evolution of Florida Cumulonimbus. Part II: Frequency Distributions of Vertical
837 Velocity, Reflectivity, and Differential Reflectivity, *Mon. Wea. Rev.*, 123,
838 1941-1963,
839 [https://doi.org/10.1175/1520-0493\(1995\)123<1941:TDKAME>2.0.CO;2](https://doi.org/10.1175/1520-0493(1995)123<1941:TDKAME>2.0.CO;2), 1995.
- 840 Zhang, Y., Li, J., Yu, R., Zhang, S., Liu, Z., Huang, J., and Zhou, Y.: A Layer-Averaged
841 Nonhydrostatic Dynamical Framework on an Unstructured Mesh for Global and
842 Regional Atmospheric Modeling: Model Description, Baseline Evaluation, and
843 Sensitivity Exploration, *J. Adv. Model. Earth Sy.*, 11, 1685-1714,
844 <https://doi.org/10.1029/2018MS001539>, 2019



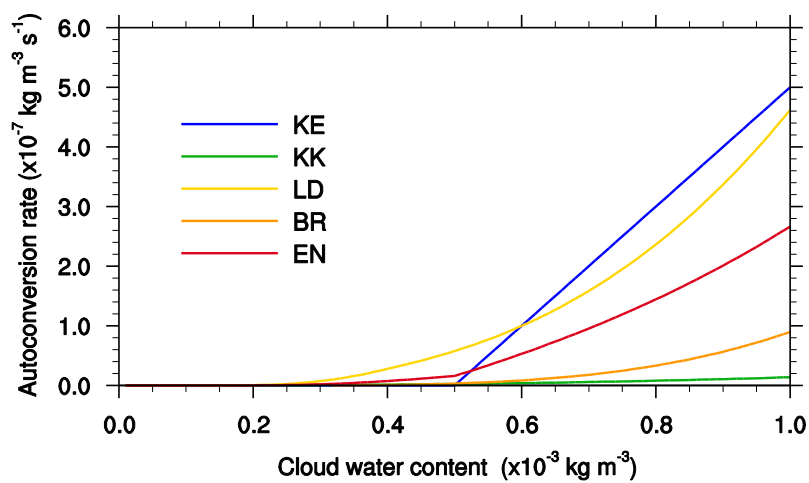
856

Figures



857

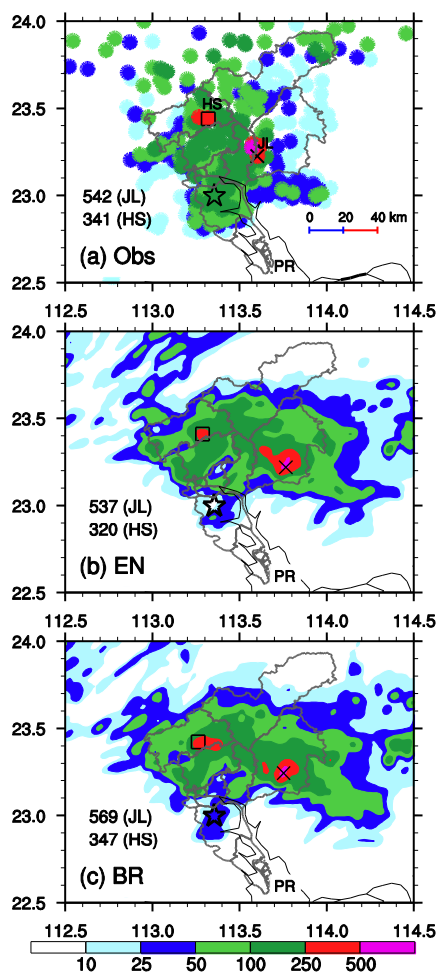
858 **Fig. 1** Evolution of autoconversion rates with a wide range of cloud water
859 content at given cloud number concentrations (N_c) of 100 cm^{-3} , 300 cm^{-3} , and 500
860 cm^{-3} , respectively. (a) KE denotes the Kessler scheme (1969), and (b) BR indicates
861 the Berry and Reinhardt scheme (1974); (c) KK and (d) LD represents the
862 Khairoutdinov and Kogan (2000) and Liu et al. (LD) schemes (2006), respectively.



863

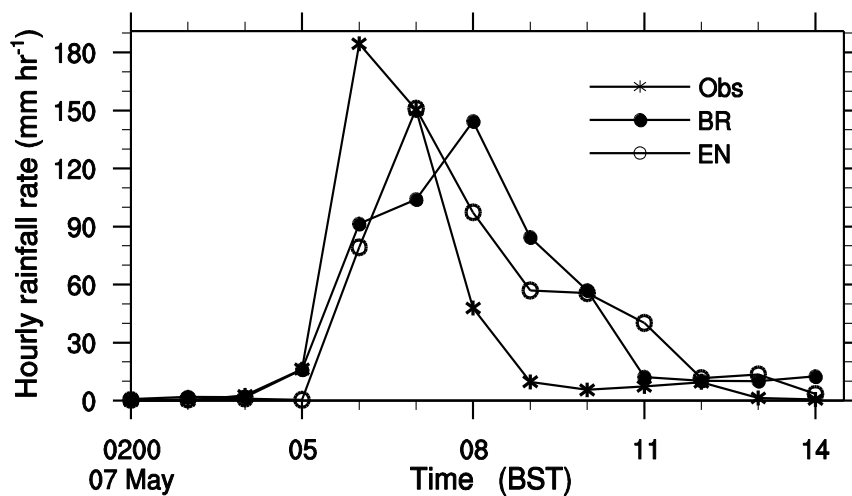
864 **Fig. 2** Comparisons of the EN scheme with the selected KE, BR, KK, and LD

865 schemes at a fixed N_c of 300 cm^{-3} . (see text for further details)



866

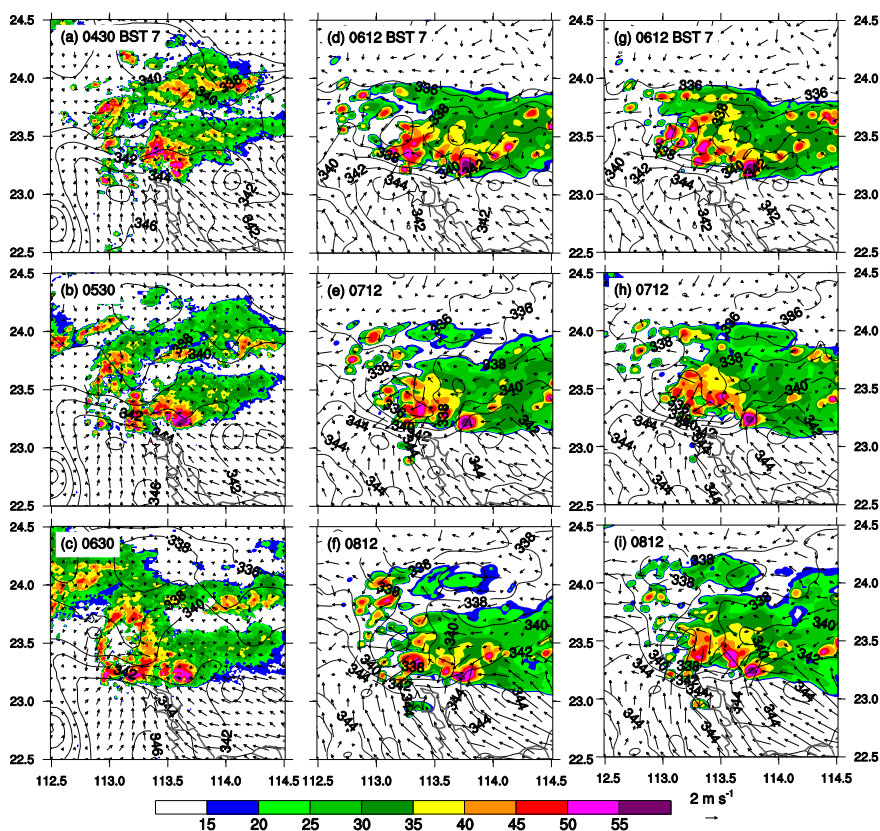
867 **Fig. 3** Spatial distribution of the 18-h accumulated rainfall during the period of
868 2000 BST 6 May to 1400 BST 7 May, 2017: (a) rain gauge observations and (b-c)
869 simulations with the EN and BR autoconversion schemes. A cross sign (×) and a
870 square sign (□) denote the locations where maximum hourly rainfall rates were (a)
871 observed or (b-c) simulated near Jiulong (JL) and Huashan(HS), respectively. The
872 values marked with JL and HS indicate the 18-h maximum accumulated rainfall
873 amounts near the JL and HS, respectively. A star indicates the city center of Guangzhou,
874 and the Pearl River is marked by PR; similarly for the rest of figures.



875
876
877

Fig. 4 Time series of hourly rainfall rates (mm hr^{-1}) from rain gauge observations

878 (asterisks) and simulated with the EN scheme (circles) and the BR scheme (dots) near
879 Jiulong during the period of 2000 BST 6 - 1400 BST 7 May 2017. (see Fig. 3 for their
880 locations)

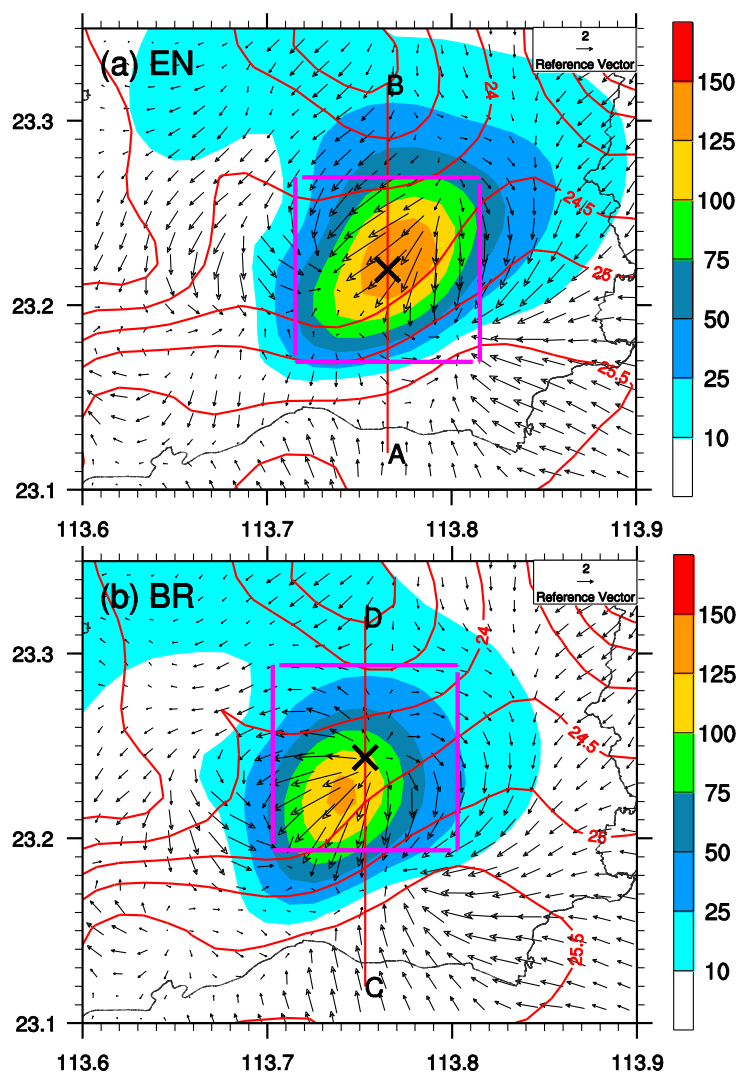


881

882 **Fig. 5** Horizontal maps of composite radar reflectivity (dBZ, shadings) and surface
883 ($z = 10$ m) horizontal wind vectors and equivalent potential temperature (θ_e , contoured
884 at 2K intervals) during the extreme rainfall stage: (a-c) observed, (d-f) simulated with
885 the EN scheme, and (g-i) simulated with the BR scheme. A reference wind vector is
886 given beneath the right column next to the composite radar reflectivity color scale.



887



888

889

Fig. 6 Spatial distribution of hourly rainfall amount (mm, shadings), temporal-averaged surface temperature (contoured at 0.5°C intervals) and horizontal wind fields (vectors) during the period from 0600 BST to 0700 BST 7 May, 2017. The red lines, A-B and C-D, indicate the locations of the vertical cross section in Fig. 7. The two pink-squared boxes, covering an area of $0.1^\circ \times 0.1^\circ$ with the center of the maximum hourly rainfall, are marked for domain-averaged in Fig. 8 and Fig. 9.

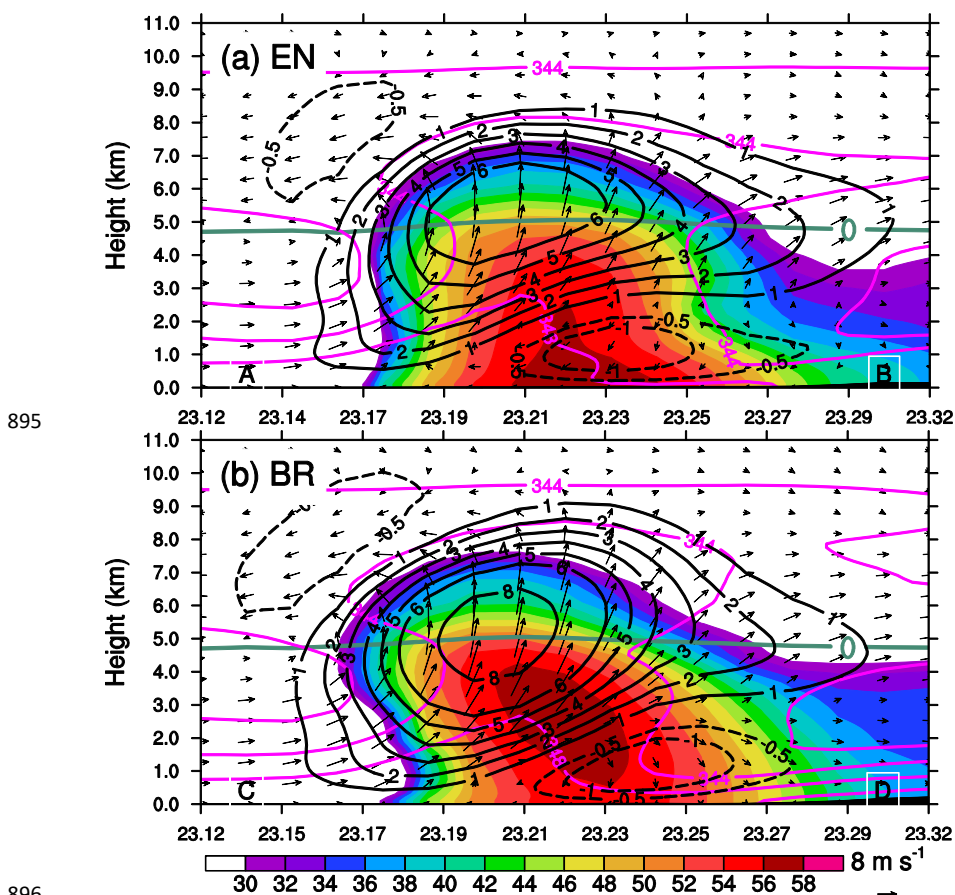
890

891

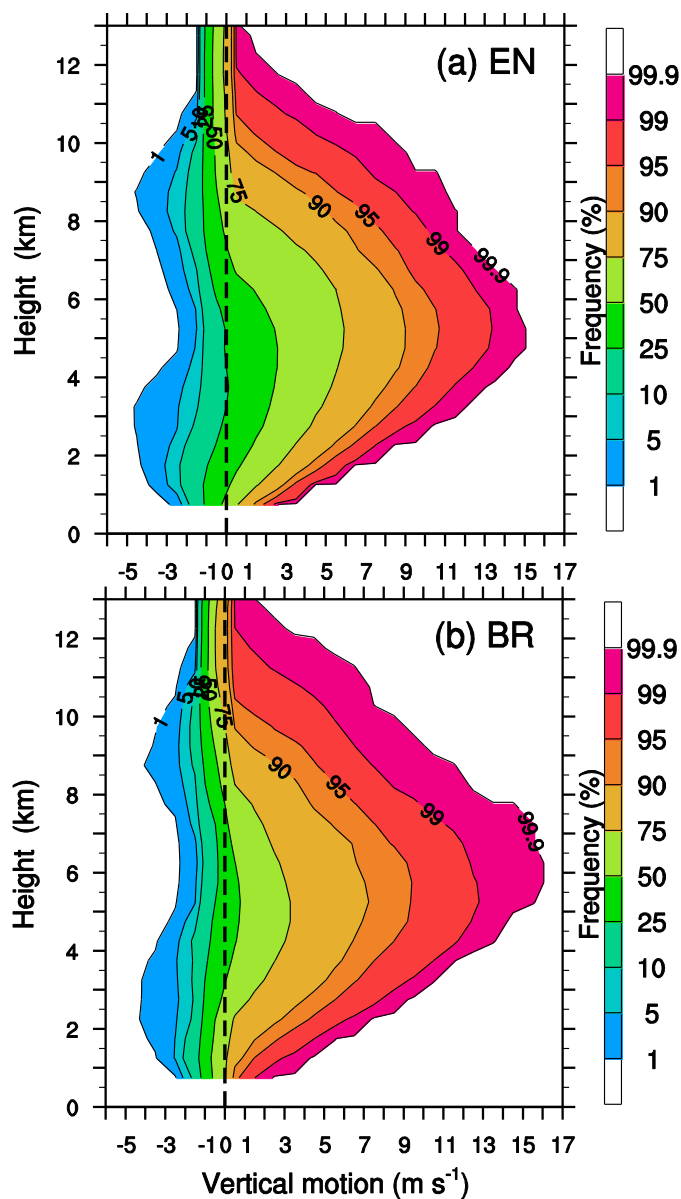
892

893

894



896
897 **Fig. 7** Temporal-averaged vertical cross sections along (a) A-B and (b) C-D in Fig.
898 6 of the simulated reflectivity (dBZ, shadings), vertical velocity (black contours, m s^{-1}),
899 in-plane flow vectors (vertical motion amplified by a factor of 2), and theta-e (θ_e ,
900 pink-contoured at 4K intervals) during the period from 0600 BST to 0700 BST 7 May,
901 2017. Thick light green line indicates an isotherm of 0°C .



902

903

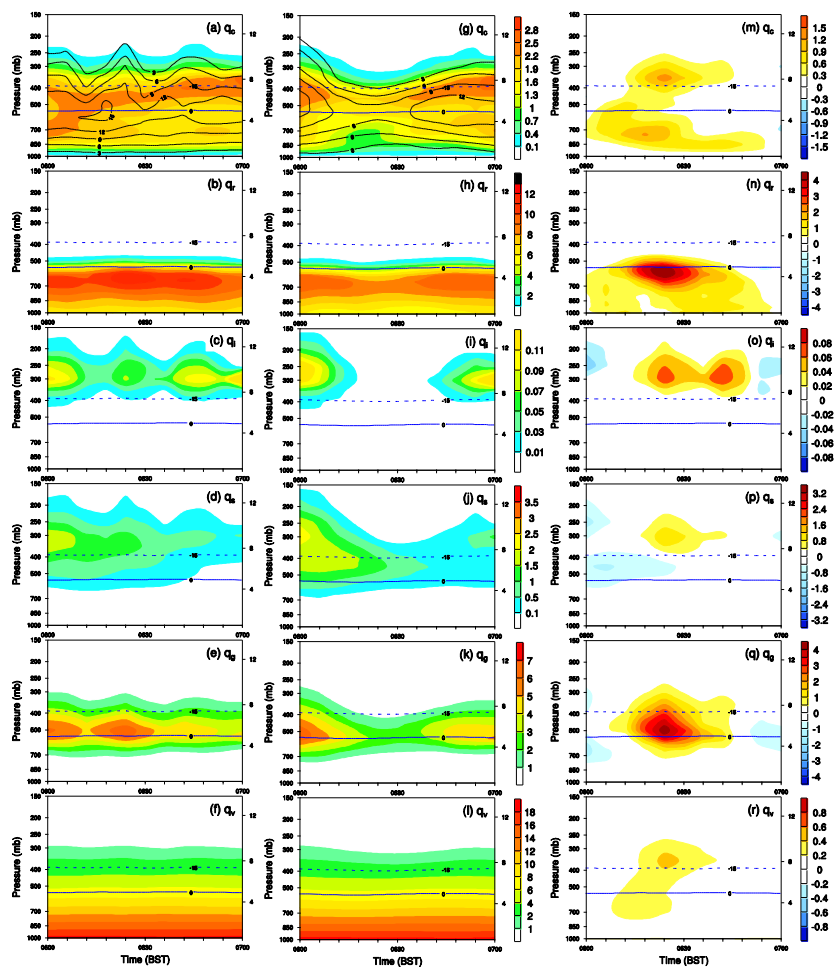
904

905

906

907

Fig. 8 CCFADs of the simulated vertical motion for (a) the EN scheme and (b) the BR scheme within the respective boxes marked with pink lines in Fig. 6. The CCFADs are calculated from eleven model outputs with six-minute intervals during the severe rainfall episode from 0600 BST to 0700 BST 7 May, 2017.



908

909 **Fig. 9** Comparison of time-height cross sections of domain-averaged mixing ratios
 910 between the EN scheme (a-f) and the BR scheme (g-i) during the period from 0600
 911 BST to 0700 BST 7 May, 2017, within the domains marked with pink lines in Fig. 6.
 912 q_c , q_r , q_i , q_s , and q_g denotes cloud water, rainwater, cloud ice, snow, and graupel,
 913 respectively. (m-r) gives the differences between EN and BR (i.e. EN – BR). Thick
 914 blue lines indicate isotherm of -15°C and 0°C , respectively.